Thin film combinatorial sputtering of Al-Ce alloys: Investigating the phase separation of asdeposited solid solutions and determining the coefficient of thermal expansion

Reece Emery<sup>1</sup>, Orlando R. Rios<sup>1</sup>, Michael J. Thompson<sup>1</sup>, David Weiss<sup>2</sup>, Philip D. Rack<sup>1,3,\*</sup>

- 1. Department of Materials Science and Engineering, University of Tennessee, Knoxville, Tennessee 37996, USA
- 2. Eck Industries, Manitowoc, Wisconsin 54220, USA
- 3. University of Tennessee Oak Ridge Innovation Institute, Knoxville, Tennessee 37996, USA

Keywords: combinatorial sputtering, thin films, rare earth alloys and compounds, thermal expansion, x-ray diffraction

## **Abstract**

 $Al_xCe_{100-x}$  thin films with a composition range of ~75.0<x<99.5 at. % (36.5<x<97.5 wt. %) were synthesized via combinatorial co-sputtering from an Al and an Al<sub>50</sub>Ce<sub>50</sub> target. The crystal structure, phase fraction, film morphology, electrical resistivity, and temperature-dependent coefficients of thermal expansion (CTE) are all correlated to the Al<sub>x</sub>Ce<sub>100-x</sub> composition. The as-deposited films form a metastable solid-solution, and annealing leads to the formation of the thermodynamically stable two-phase system of Al and the α-Al<sub>11</sub>Ce<sub>3</sub> intermetallic. Temperature dependent x-ray diffraction (XRD) reveals that the two phases expand independently of one another, and the thin film Al temperature-dependent CTE is similar to bulk Al. The thin film Al<sub>11</sub>Ce<sub>3</sub> intermetallic phase has a nearly constant CTE of ~1.5x10<sup>-5</sup>/°C within the temperature range studied (25-550°C). To confirm the thin film Al<sub>11</sub>Ce<sub>3</sub> results, bulk stoichiometric Al<sub>11</sub>Ce<sub>3</sub> and +/- 1 wt.% Ce samples were prepared and the CTE of each was measured with the same conditions. A Rietveld analysis of the bulk data enabled an estimation of the CTE in each of the 3 orthorhombic lattice parameters, which displayed anisotropic behavior. The thin film and bulk CTE measurements were in very good agreement. Estimations of the temperature dependent CTE of the two-phase alloys are made via the Reuss and Voigt models. By demonstrating the efficacy of the approach, more complex multi-component rapid materials discovery of low CTE Al-alloys can be pursued via the combinatorial thin film synthesis and XRD measurement.

### 1. Introduction

Alloying aluminum with cerium in the range of 6-16 wt. % (1.2-3.5 at. %) has recently been shown to significantly improve the high temperature mechanical properties, castability, and thermal stability relative to existing aluminum alloys [1,2]. Traditional aluminum alloys have been of interest in the automotive industry where factors such as weight, high-temperature performance, and cost play an important role in determining attainable fuel efficiency. Existing aluminum alloys meet the weight and cost requirements; however, they lack the necessary high-temperature performance required as the demand for higher power throughput and fuel efficiency continues to increase. Cerium-based aluminum alloys have been shown to maintain the weight

<sup>\*</sup>corresponding author: prack@utk.edu

and cost-savings of traditional aluminum alloys while providing high-temperature stability due to the formation of intermetallic phases [3–5]. Recently, the Al-Ce alloy system has also been of interest as a surface coating for corrosion resistance [6,7] where it has been shown that the Al-Ce alloy system creates a Ce-rich outer passivation layer, which limits the reduction of the Al matrix [8].

Al has a face-centered cubic (FCC) structure with a lattice parameter of 4.04 Å [9]. Cerium has been shown to crystallize in two forms at ambient temperatures and pressure. One is an FCC structure with a lattice parameter of 5.14 Å while the other is a hexagonal close-packed (HCP) structure with a=3.65 Å, and c= 5.91 Å [10]. This leads to limited solubility in the alloy system. However, the system readily forms several intermetallics. In the composition region of interest, (<21.5 at.% Ce), the Al-Ce alloy system forms a two phase region with a pure Al matrix and the  $\alpha$ Al<sub>11</sub>Ce<sub>3</sub> intermetallic.  $\alpha$ Al<sub>11</sub>Ce<sub>3</sub> forms an orthorhombic structure with a=4.39 Å, b=10.08 Å, and c=13.02 Å [11].

The coefficient of thermal expansion (CTE) is an important parameter in high temperature applications as the change in dimension with temperature affects operational tolerances and if excessive, can lead to failure. Additionally, for parts that have cyclic temperatures, the induced thermal stresses can cause thermal fatigue. Temperature-dependent x-ray diffraction (XRD) is one technique that can be used to quantify the CTE of a material. In this technique, the CTE is determined through changes in the interplanar spacing with changes in temperature [12]. Using this technique, it has been shown that the CTE decreases with increasing grainsize [13], and that various phases can be measured simultaneously [14]. Furthermore, CTE anisotropy has been explored by comparing various reflections in non-cubic systems [15,16].

Combinatorial sputtering can be leveraged as a convenient tool for rapid material discovery as it can achieve thin film compositions that cover a large and targeted composition range. Further, the high energy deposition process and fast cooling rates allows for the realization of metastable material configurations, for example supersaturated solid solution found in various as-deposited sputtered alloys [17,18]. Subsequent annealing can be utilized to achieve the equilibrium state of the system through recrystallization, grain growth, and phase separation [19,20]. The motivation of the study is to demonstrate that thin film combinatorial synthesis can be used for alloy development. In particular, we apply the thin film rapid materials discovery approach to a new alloy system (Al<sub>x</sub>Ce<sub>100-x)</sub> that is being explored for various lightweight alloy applications. The coefficient of thermal expansion (CTE) is a critical property to various high-temperature applications and thus we use the thin film approach to extract the CTE of the Al<sub>11</sub>Ce<sub>3</sub> intermetallic to determine its suitability. Thus, a combinatorial library of Al<sub>x</sub>Ce<sub>100-x</sub> (~75.0<x<99.5 at. %) alloys is co-sputter deposited and the crystal structure and phase fraction, film morphology, effective electrical resistivity, and temperature-dependent coefficients of thermal expansion are all correlated to the Al<sub>x</sub>Ce<sub>100-x</sub> composition.

# 2. Material and methods

## 2.1 Sputtering Conditions

 $Al_xCe_{100-x}$  alloys were co-sputtered from a pure Al and a  $Al_{50}Ce_{50}$  (50-50 at.%) target to form a combinatorial library across a  $SiO_2$ -coated (500 nm) Si substrate (500 $\mu$ m). The substrate was fixed and not rotated to generate the composition gradient. The Al target was powered with a 200 W DC source while the  $Al_{50}Ce_{50}$  target was powered with a 100 W RF source in a 5 mTorr Ar ambient atmosphere for 2 hours.

### 2.2 X-Ray Conditions

Room temperature x-ray diffraction (XRD) patterns were measured using a Malvern Panalytical X'Pert3 MRD diffractometer while temperature-dependent XRD experiments were performed using a Malvern Panalytical Empyrean diffractometer. A  $2\theta$ -  $\Omega$  scan with an  $\Omega$  offset of 3° with a Cu tube ( $\lambda$ =0.154 nm) was used for all experiments. Room temperature XRD experiments on an as-deposited and an annealed sample were run with an angle sweep from  $25^{\circ}$  to  $85^{\circ}$  with a step size of  $0.52^{\circ}$  (total time of each scan 30 min). To estimate the coefficient of thermal expansion, we performed temperature-dependent x-ray diffraction experiments with an angle sweep from  $20^{\circ}$  to  $110^{\circ}$  with a  $0.26^{\circ}$  step size (total time of each scan 23 min). The sample was heated *in situ* from room temperature ( $\sim$ 25°C) to  $550^{\circ}$ C in a nitrogen atmosphere with a heating rate of  $5^{\circ}$ C/min. The sample was held for 5 minutes at 100, 200, 300, 400, 500, and  $550^{\circ}$ C after which each XRD measurement was taken. The same conditions were used during the cooling cycle. In total, thirteen measurements were taken for each temperature cycle.

### 2.3 Annealing Conditions

Annealing was conducted in vacuum with a base pressure of  $\sim 3x10^{-7}$  Torr. The sample was ramped from room temperature ( $\sim 15^{\circ}$ C) to  $500^{\circ}$ C over a period of 1 hour. It was held at  $500^{\circ}$ C for 10 minutes and then reduced to  $475^{\circ}$ C and  $450^{\circ}$ C and held for 5 and 15 minutes, respectively. The sample was cooled at a rate of  $10^{\circ}$ C/min from  $450^{\circ}$ C to  $200^{\circ}$ C at which point the heater was turned off and the sample was left to cool to room temperature overnight.

### 2.4 Scanning Electron Microscopy and Energy dispersive X-ray spectroscopy

Energy dispersive x-ray spectroscopy (EDXS) and scanning electron microscopy (SEM) were conducted on a Carl Zeiss MERLIN SEM. The combinatorially sputtered  $Al_xCe_{100-x}$  thin film (as-deposited and annealed) was measured at 9 points at equally spaced increments of 10 mm along the composition gradient. An accelerating voltage of 10 keV was used for EDXS.

#### 2.5 4-Point Probe Measurements

Resistivity measurements were performed using a Lucas Labs Pro4-440N QuadPro Resistivity System with a Keithley 2400 Source Measurement Unit. Resistivity was calculated by multiplying the experimental resistance measurement by the film thickness. Film thickness values were taken from the simulated thickness profile in figure 1d.

# 3. Results and Discussion

#### 3.1 Full Wafer Characterization

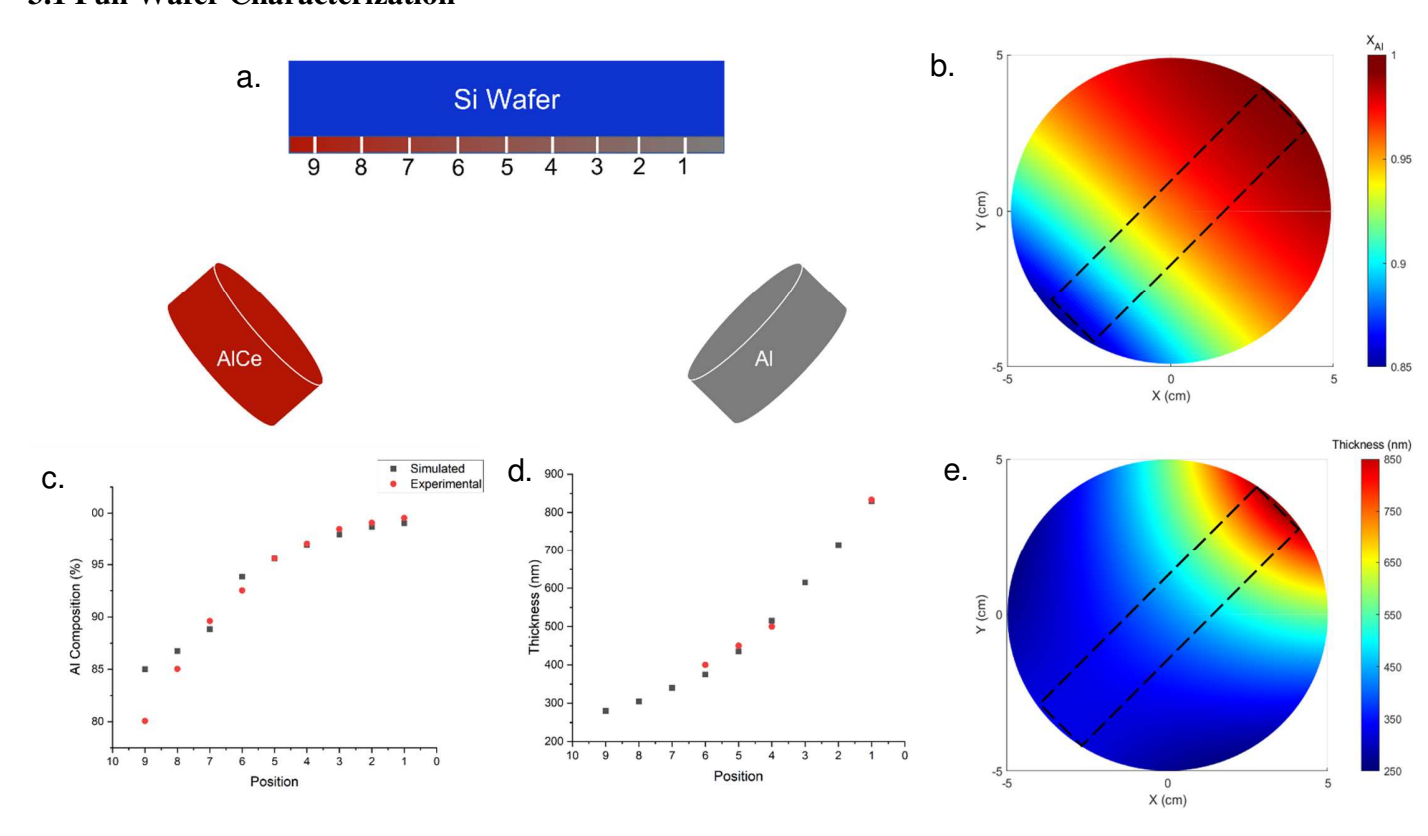


Figure 1: (a) Schematic of sputtering configuration. (b) Simulated Al composition of the Al-Ce combinatorially sputtered 100 mm diameter film. Comparison of simulated versus experimental (c) composition and (d) thickness. (e) Simulated film thickness of the Al-Ce combinatorially sputtered 100 mm diameter film. Dashed black box denotes area of study.

Figure 1a is a schematic of the sputtering configuration used to synthesize the Al<sub>x</sub>Ce<sub>100-x</sub> thin films. Since the substrate is not rotated and the flux from the targets are different, both a composition and thickness gradient are generated, respectively. For reference, position 0 is at the aluminum rich wafer edge and positions 1-10 proceed in 10 mm increments across the wafer diameter along the gradient to the Ce-rich wafer edge. Figure 1b also illustrates the simulated [21] Al composition across the entire substrate and 1c) the simulated versus experimental EDXS measured film composition and the 1d) simulated and SEM measured thickness along the gradient diameter centerline. The simulations assumed a substrate center (position 5) Al and Al<sub>50</sub>Ce<sub>50</sub> deposition rate of 3 and 0.75 nm/min, respectively. Figure 1c and 1d show good agreement between the experimental and simulated composition and thickness, respectively. Figure 1e shows the complementary thickness as a function of the substrate position for the entire substrate.

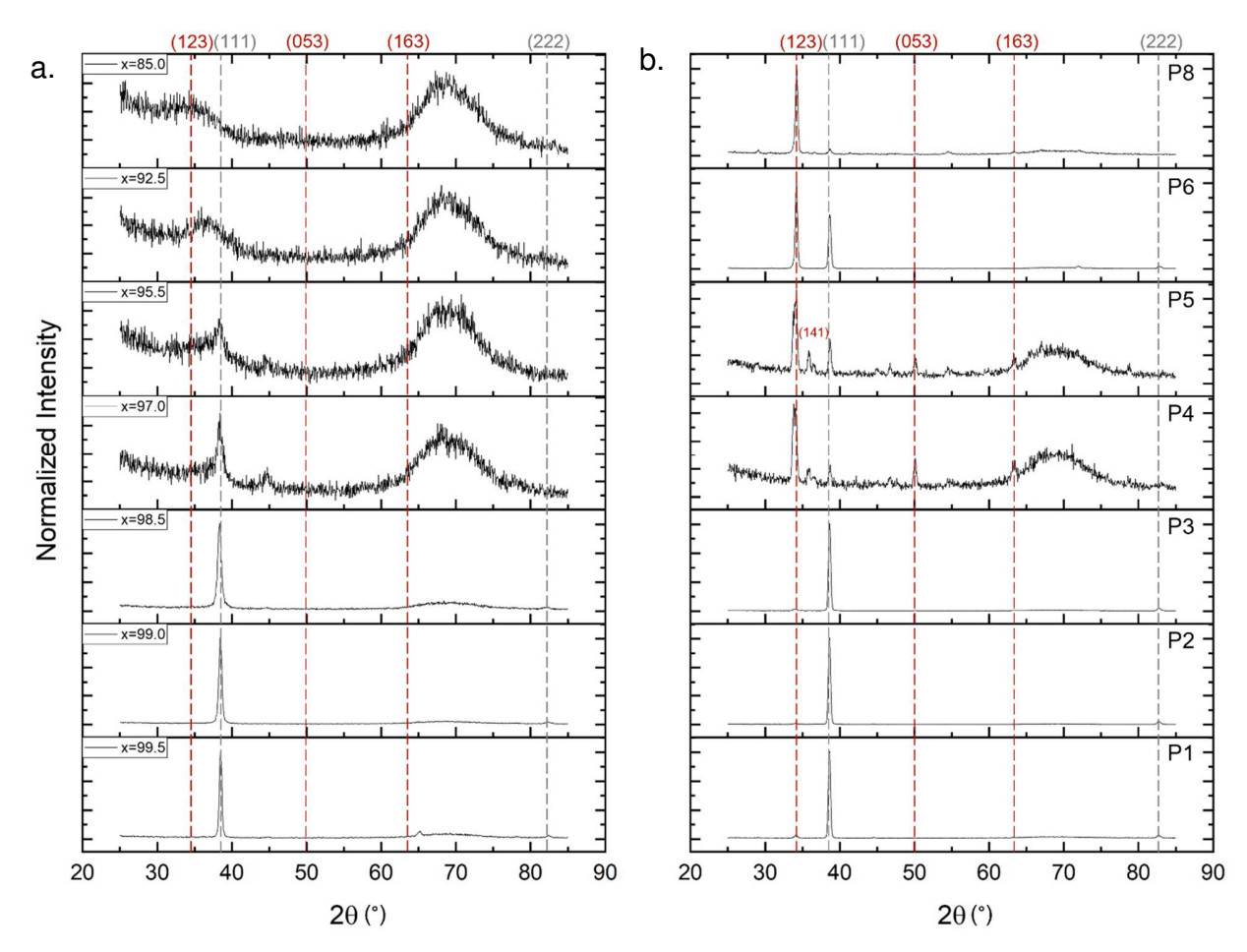


Figure 2:XRD results for  $Al_xCe_{100-x}$  films for (a) as-deposited and (b) annealed samples. Grey lines denote Al peaks. Red lines denote  $Al_{11}Ce_3$  peaks [22]

To confirm the crystal structure of the as-deposited and annealed combinatorially sputtered Al<sub>x</sub>Ce<sub>100-x</sub> thin films, x-ray diffraction (XRD) was conducted at positions 1-6 (starting at 10 mm from the Al-rich edge and measuring every 10 mm) and position 8 as shown in Figure 2. For x>97.0, the Al (111) reflection dominates with trace reflections of the (222) plane. A shift in 2θ and broadening in the Al (111) peak suggests the formation of a metastable solid solution for the as-deposited sample, which appears evident up to position 5 (x=95.5). For  $x \le 97$  (or approximately the hypereutectic region) the x-ray intensity drops as evidenced by the low signal to noise. A broad amorphous hump emerges at  $\sim 70^{\circ}$  and is attributed to the amorphous Al<sub>11</sub>Ce<sub>3</sub> phase, which has reasonable phase fraction in this region. The Al<sub>11</sub>Ce<sub>3</sub> is fairly refractory as it has an incongruent phase transformation to Al<sub>4</sub>Ce and Al<sub>3</sub>Ce at ~1000°C [23], thus the rapid solidification that occurs during the sputtering process inhibits crystallization of this phase at room temperature. The Al (111) peak is very broad and shifted to lower  $2\theta$  up to x=95.5 consistent with the solid solution formation; at x > 92.5 it is unclear if there is any long range order in the material as the phase fraction is dominated by the Al<sub>11</sub>Ce<sub>3</sub> which appears to be amorphous. To confirm the observed results as-deposited results are consistent with no phase

separation EDS maps of various compositions were measured which confirmed the homogeneous distribution of the Al and Ce (see supplemental information 1). After annealing, the  $Al_{11}Ce_3$  intermetallic phase emerges and the peak ratio of the Al (111)/ $Al_{11}Ce_3$  (123) decreases consistent with the expected increase in the  $Al_{11}Ce_3$  phase fraction with increasing Ce content. Note that the (111) orientation in FCC crystals have a preferred orientation due to the low surface energy [24]. As-expected, the aluminum peak intensity increases, narrows, and shifts back to its expected position (higher 2 $\theta$ ) consistent with rejection of the Ce in Al phase (note confirmation of this in temperature dependent x-ray diffraction below). The recrystallization for 97.0<x<95.5 seems to be robust as the x-ray diffraction intensity for the Al (111) (for x>97) and  $Al_{11}Ce_3$  (123) (for x<95.5) peaks are high. Interestingly, the recrystallization for the x=97 and 95.5 compositions seem sluggish as the signal to noise in the diffraction data is low and the amorphous peak at ~  $70^{\circ}$  is relatively high.

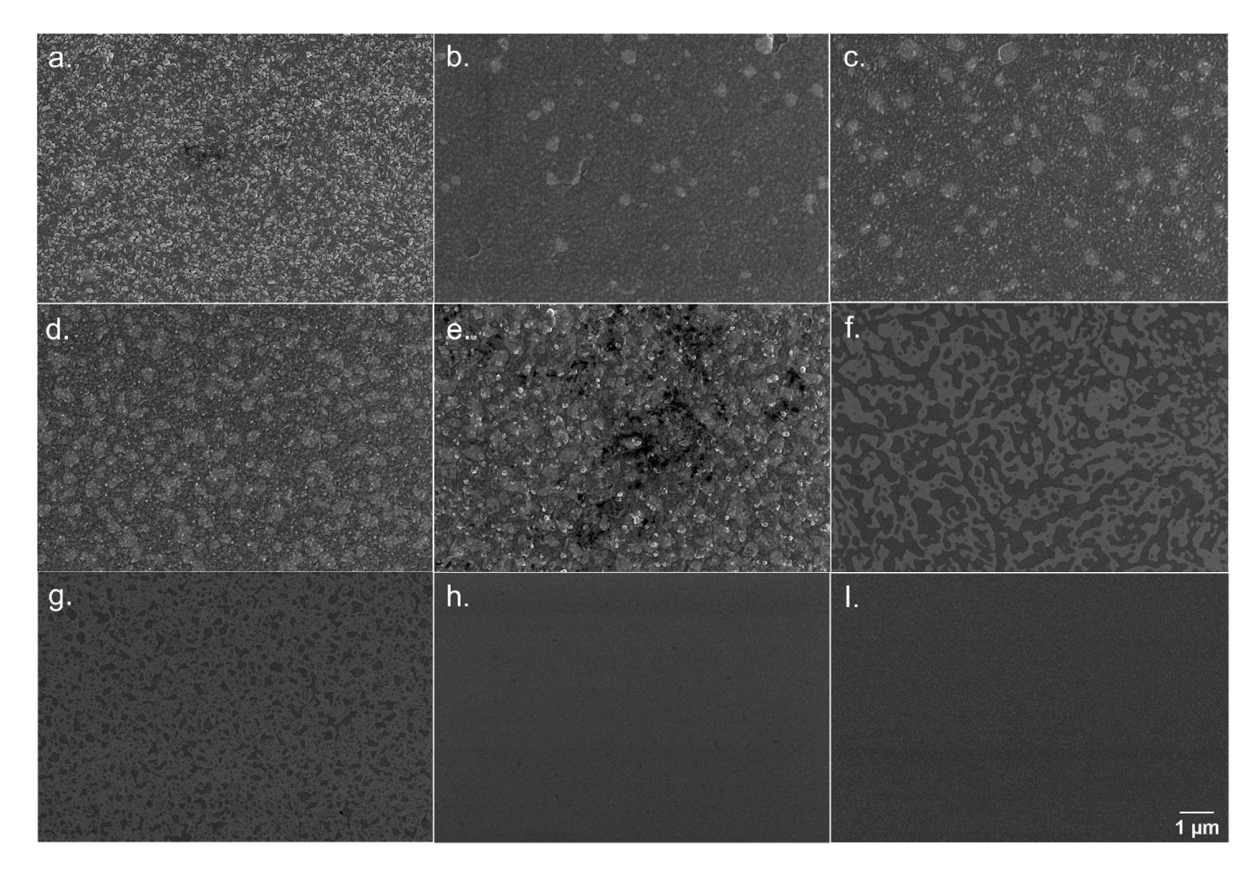


Figure 3. Plane view SEM images of the annealed films where (a)  $Al_{99.5}Ce_{0.5}$ , (b)  $Al_{99.0}Ce_{1.0}$ , (c)  $Al_{98.5}Ce_{1.5}$ , (d)  $Al_{97.0}Ce_{3.0}$ , (e)  $Al_{95.5}Ce_{4.5}$ , (f)  $Al_{92.5}Ce_{7.5}$ , (g)  $Al_{89.5}Ce_{10.5}$ , (h)  $Al_{85.0}Ce_{15.0}$ , and (i)  $Al_{80.0}Ce_{20.0}$ .

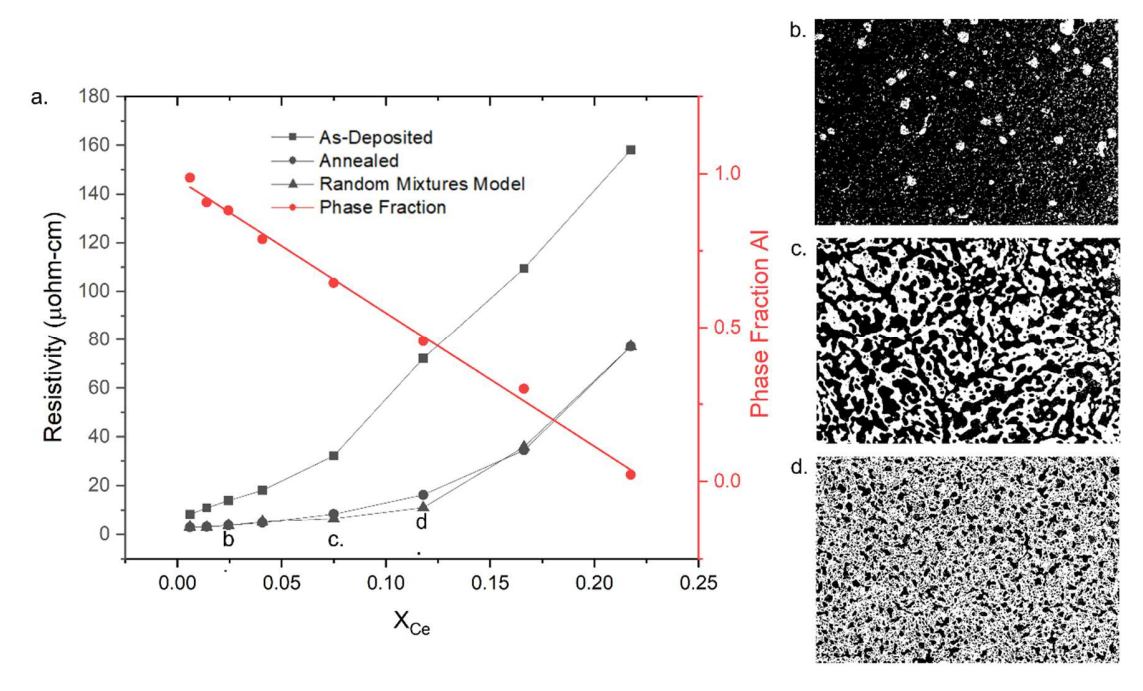


Figure 4. (a) Resistivity (left axis) and phase fraction (right axis) as a function of Cerium content for the as-deposited and annealed sample as well as the resistivity calculated via a random mixture model. Micrographs after thresholding for (b)Al<sub>98.5</sub>Ce<sub>1.5</sub>, (c) Al<sub>92.5</sub>Ce<sub>7.5</sub>, and (d) Al<sub>87.5</sub>Ce<sub>1.2.5</sub>. White regions are the Al<sub>11</sub>Ce<sub>3</sub> phase while the black regions are the Al phase

Figure 3 show the SEM images of annealed Al<sub>x</sub>Ce<sub>100-x</sub> films (see supplemental information for as-deposited films). As noted in the progression to higher Ce concentration, the emergence of a second phase with higher secondary electron yield emerges. EDS maps confirmed that the brighter second phase contains cerium and thus assigned to the equilibrium Al<sub>11</sub>Ce<sub>3</sub> phase. Clearly the phase fraction of the Al<sub>11</sub>Ce<sub>3</sub> phase fraction increases with increasing Ce content as expected and as observed in the XRD. An estimation of the phase fraction was determined via image processing and good agreement between the estimated Al<sub>11</sub>Ce<sub>3</sub> and Al phase fraction versus the phase fraction calculated from the phase diagram was obtained (see supplemental information for a plot of the estimated versus calculated phase fraction). In figure 3a the Al<sub>11</sub>Ce<sub>3</sub> is not evident in the SEM image, but small precipitate on the order of a 50-200 nm emerge in 3b and the size and number grow from 3c and 3d, respectively. The contrast in 3e shows clear precipitation, but the intergranular Al region is not as dark in the image. Note there is a significant transition in the microstructure in figure 3e to 3f where the Al<sub>11</sub>Ce<sub>3</sub> grain size increases and is interconnected. Interestingly this is consistent with the enhanced crystallization observed at higher Ce content in position 6 observed in the x-ray diffraction. This enhanced transformation at this composition will be studied in the future.

## 3.2 Resistivity Measurements

The composition and microstructure were also correlated to the resistivity as shown in figure 4. The resistivity of the as-deposited sample increases with increasing Ce content. As described above, the  $Al_xCe_{100-x}$  alloy forms a solid solution up to  $\sim x=95.5$  and at higher Ce content appears

to be in an amorphous phase. Thus, increase in resistivity in the as-deposited phase up to  $X_{Ce}$  = 4.5 is due to solid solution effects; cerium has lower resistivity than aluminum and the size mismatch strains the lattice which decreases the resistivity. Beyond that composition, the slope changes slightly and the as –deposited resistivity is that of the amorphous Al<sub>x</sub>Ce<sub>100-x</sub> phase which could be an amorphous form of sub-stoichiometric Al<sub>11</sub>Ce<sub>3</sub> (cerium deficient for 4.5<X<sub>Ce</sub><21). For the annealed sample, the resistivity increases slowly until 7.5 at. % Ce after which there is a sharp increase in the resistivity. As shown in figure 3, upon annealing, the system phase separates into a low resistivity Al phase and higher resistivity intermetallic phase. Note that because we are in a two-phase system in the annealed film, the resistivity is an effective medium approximation of the two constituent phases. In this equilibrium state, for Ce content less than 10.5 at. %, the current is carried by the percolating Al network. Image analysis revealed that at the Al<sub>92.5</sub>Ce<sub>7.5</sub> composition, the Al phase fraction is ~55%, which supports the percolating Al network. The image analysis suggests the Al phase fraction is only 38% at Al<sub>89.5</sub>Ce<sub>10.5</sub> and 5% at Al<sub>85.0</sub>Ce<sub>15.0</sub>. Thus, at aluminum concentrations higher than Al<sub>92.5</sub>Ce<sub>7.5</sub>, the current has a percolating path to travel through the aluminum phase, however as the intermetallic phase fraction increases above this concentration, the percolating network closes off thereby increasing the resistivity. A random mixtures model [25] was applied using the phase fractions estimated via the image analysis. The constituent resistivities were taken to be 2.65 μohm-cm for Al [26] and was determined experimentally to be ~77 μohm-cm for the Al<sub>11</sub>Ce<sub>3</sub> intermetallic which is consistent with literature values [27]. Very good agreement between the model and experimental phase separated resistivity values. This suggests that a random combination of series and parallel connections exist within the system and that neither phase dominates the composite resistivity value. Comparing the as-deposited versus the annealed film, it is clear that the solid solution effects increase the resistivity more than the second phase intermetallic.

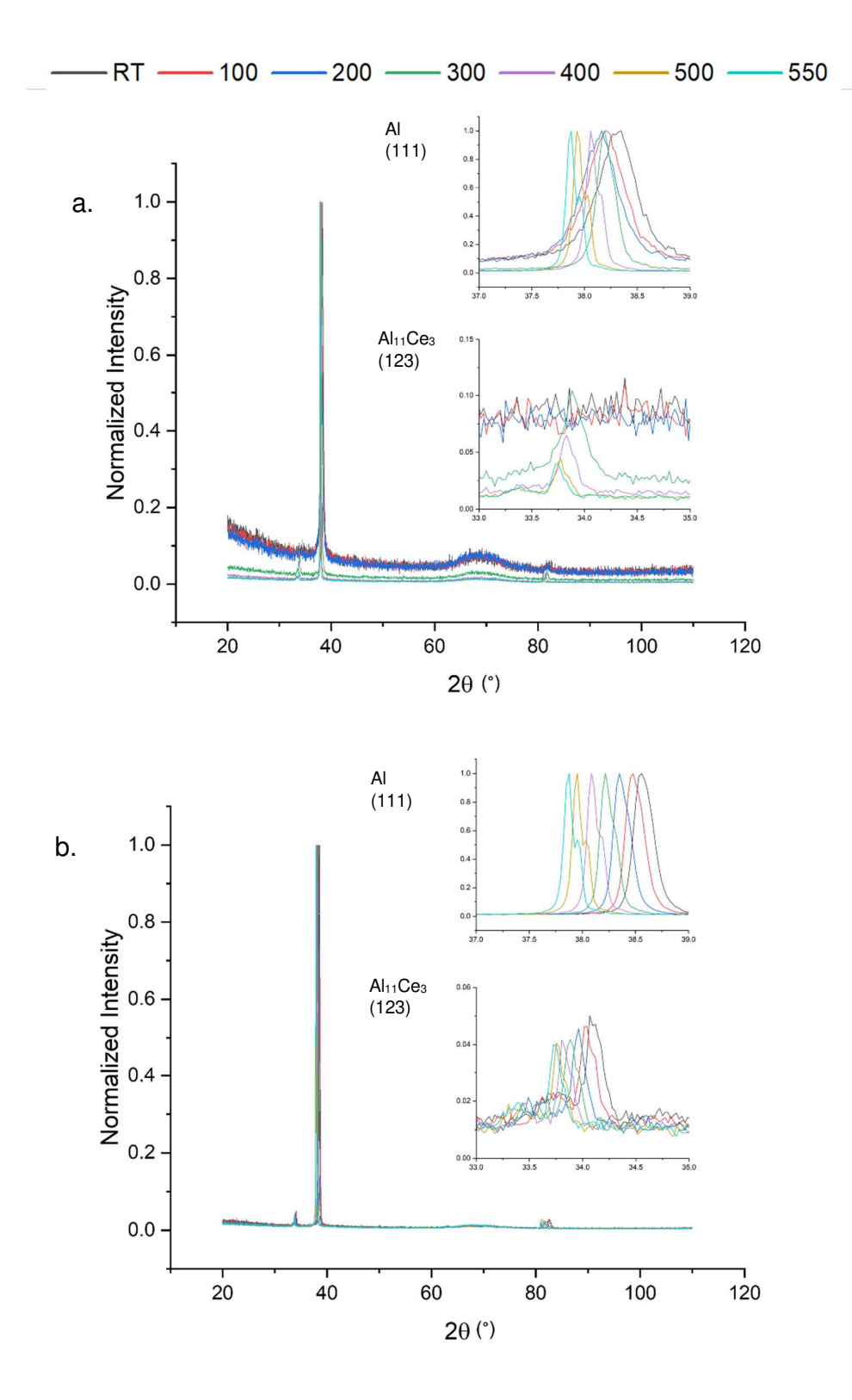


Figure 5: XRD results of the Al<sub>97</sub>Ce<sub>3</sub> composition for (a) the heating cycle from room temperature to 550°C, and (b) the cooling cycle from 550°C back to room temperature. Inset are the normalized Al (111) peaks, and the Al<sub>11</sub>Ce<sub>3</sub> intermetallic peaks.

## 3.3 High Temperature X-ray Diffraction Measurements

Figure 5 shows the overlay of the x-ray diffraction results for the Al<sub>97</sub>Ce<sub>3</sub> composition (position 4) during a 5a temperature ramp and 5b cool down. Consistent with figure 2, there are three predominant peaks. Around 34° is a low angle peak associated with the (123) Al<sub>11</sub>Ce<sub>3</sub> phase. The Al (111) peak is present at ~38° as well as the Al (222) peak at ~82°. In the as-deposited state, up to 200°C, the material is in the metastable solid solution. At the 300°C anneal step, the Al<sub>11</sub>Ce<sub>3</sub> (123) starts to precipitate from the solid solution and the Al (111) and (222) reflection intensities increase. Throughout the annealing process, the peaks shift and sharpen. Inset in figure 5a and 5b are magnified views of the Al (111) and the Al<sub>11</sub>Ce<sub>3</sub> (123) normalized peaks for the heating cycle and cooling cycle, respectively. Figure 6 illustrates the resultant Al (111) interplanar spacing during the heating and cooling cycle. As is shown, during the heating cycle, the Al (111) interplanar spacing increases from room temperature to 100°C consistent with thermal expansion and from 100 to 300°C it saturates and decreases, suggesting intrinsic stress relief in the film. As noted above, at 300°C, the Al<sub>11</sub>Ce<sub>3</sub> phase emerges consistent with figure 2. From 300°C to 550°C the peaks shift consistent with thermal expansion and as shown in figure 6 during the cooling cycle the Al<sub>11</sub>Ce<sub>3</sub> (123) interplanar spacing contracts linearly with decreasing temperature. The open hysteresis observed in the heating/cooling cycle for the Al (111) is a measure of the stress relief and rejection of the Ce in the solution, which also leads to a lattice contraction as shown in figure 6. The total contributions can be estimated by comparing the interplanar spacing of the asdeposited film to the room temperature value after the temperature cycle. A simple calculation of the lattice expansion from a Vegard's law approximation suggests that substitutional Ce induces ~564 MPa of tensile stress to the Al lattice at this concentration. Thus, the difference in the room temperature interplanar spacing before and after the annealing cycle is due to the Al<sub>11</sub>Ce<sub>3</sub> precipitation and ~ -109 MPa (compressive) stress is due to stress relief. Similarly, a Vegard's law approximation of the Al<sub>99.5</sub>Ce<sub>0.5</sub> composition was calculated suggesting that (94 MPa) of the difference in room temperature interplanar spacing is due to the Al<sub>11</sub>Ce<sub>3</sub> precipitation and ~ 76 MPa (tensile) is due to stress relief. A Vegard's law approximation could not be performed on the Al<sub>92.5</sub>Ce<sub>7.5</sub> composition as the HTXRD experiment was run on a preannealed sample. The interplanar spacing values of the Al<sub>11</sub>Ce<sub>3</sub> precipitation phase is also shown on figure 6. Because all the data was consistent, only a single dashed line representing the linear regression is shown. As discussed below, we use the cooling cycle data to extract the coefficient of thermal expansion of the Al and Al<sub>11</sub>Ce<sub>3</sub> phases in the thin films.

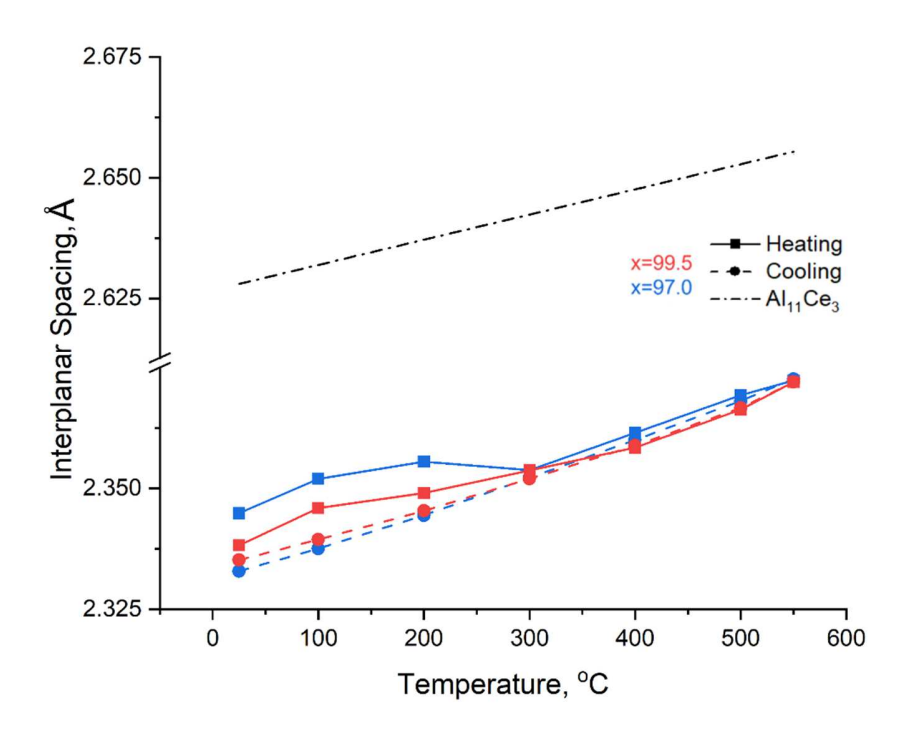


Figure 6. Measured interplanar spacing for the Al (111) peak measured during heating and cooling, and  $Al_{11}Ce_3$  (123) peak upon cooling for  $Al_{99,5}Ce_{0.5}$  and  $Al_{97}Ce_3$ .

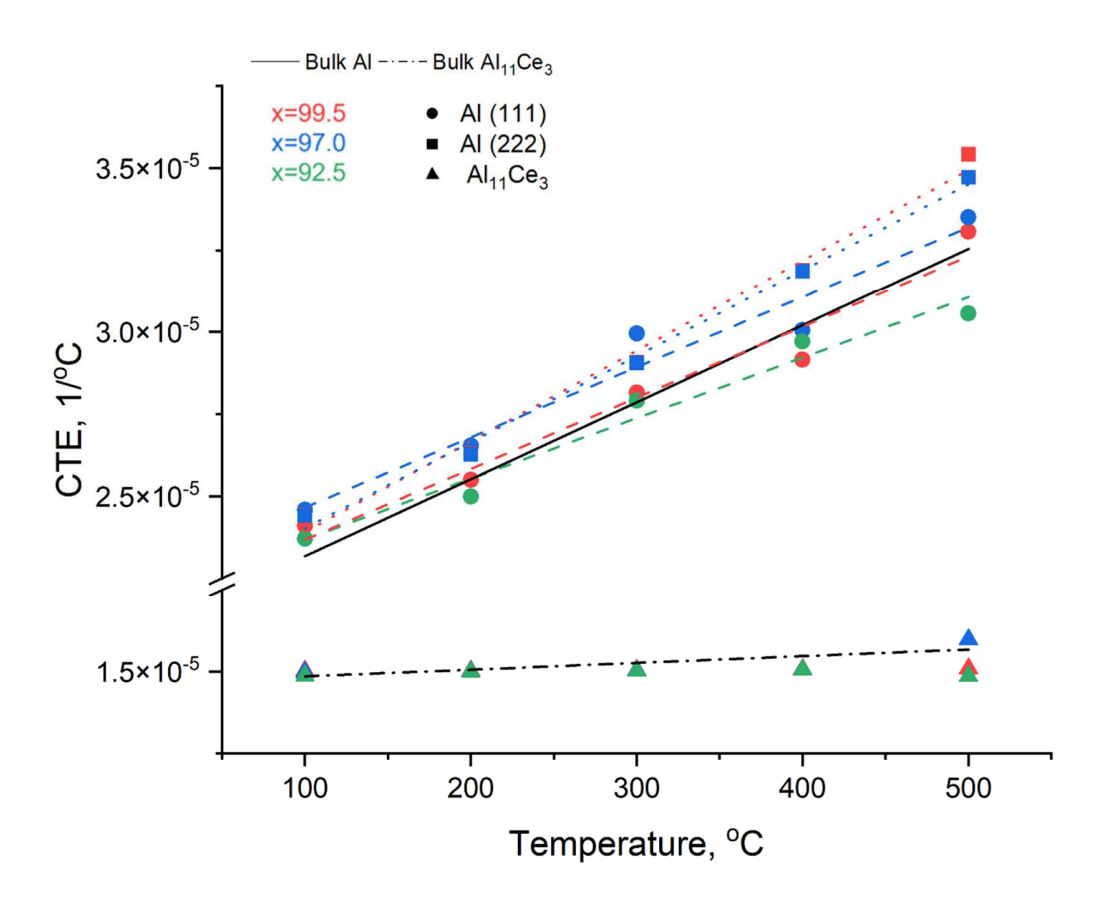


Figure 7: CTE calculated (with correction for x=92.5) from HTXRD experiments for the Al (111), Al (222), and  $Al_{11}Ce_3$  (123) showing the temperature dependent CTE compared to bulk Al and  $Al_{11}Ce_3$  for each composition measured

## 3.4 Coefficient of Thermal Expansion Determination

The coefficient of thermal expansion (CTE) can be calculated through the shifts in the XRD peaks as a function of temperature. The linear coefficient of thermal expansion can be calculated using:

$$\frac{\Delta d}{d} = \alpha \Delta T$$
 (1)

where d is the interplanar spacing determined via Braggs law,  $\alpha$  is the CTE, and  $\Delta T$  is the change in temperature. Using this equation and estimating  $\Delta d/d$  for each temperature increment, the temperature dependent CTE for aluminum and  $Al_{11}Ce_3$  can be estimated. Because of the rigid underlying  $SiO_2$  on Si substrate, below a critical thickness a correction can be performed to account for the in-plane biaxial compressive stress that develops due to the difference in the  $SiO_2$  and Al CTE [9]. The correction term is given by:

$$\alpha' = \frac{\alpha_{f} - \alpha_{sub}}{1 - v}$$
 (2)

where  $\alpha$ ' is the uncorrected CTE,  $\alpha_f$  is the CTE of the film (Al),  $\alpha_{sub}$  is the CTE of the substrate (SiO<sub>2</sub>), and  $\nu$  is Poisson's ratio.  $\alpha_{sub}$  (SiO<sub>2</sub>) is taken to be 0.25\*10<sup>-6</sup>/°C [28], and  $\nu$  is taken to be 0.33 for Al. The cooling cycle data was used to determine the CTE values as the intrinsic stress is relieved and the equilibrium phases have formed.

Note that for the high Ce content sample (x=92.5) the measured CTE values were adjusted using equation 2. The thickness value at this point is ~375 nm as shown in figure 1d. In this thickness regime, the CTE value shows a dependence due to the rigid nature of the substrate [29]. Both the Al and Al<sub>11</sub>Ce<sub>3</sub> phase exhibit this thickness dependent behavior. As shown in figure 7, the two phases expand independently of one another at each composition. The temperature dependent CTE of the Al matrix within the thin films increases similarly to bulk Al and the values for Al found in literature [30]. However, the Al<sub>11</sub>Ce<sub>3</sub> intermetallic phase has a nearly constant CTE of ~1.5x10<sup>-5</sup>/°C within the temperature range on this study (25-550°C).

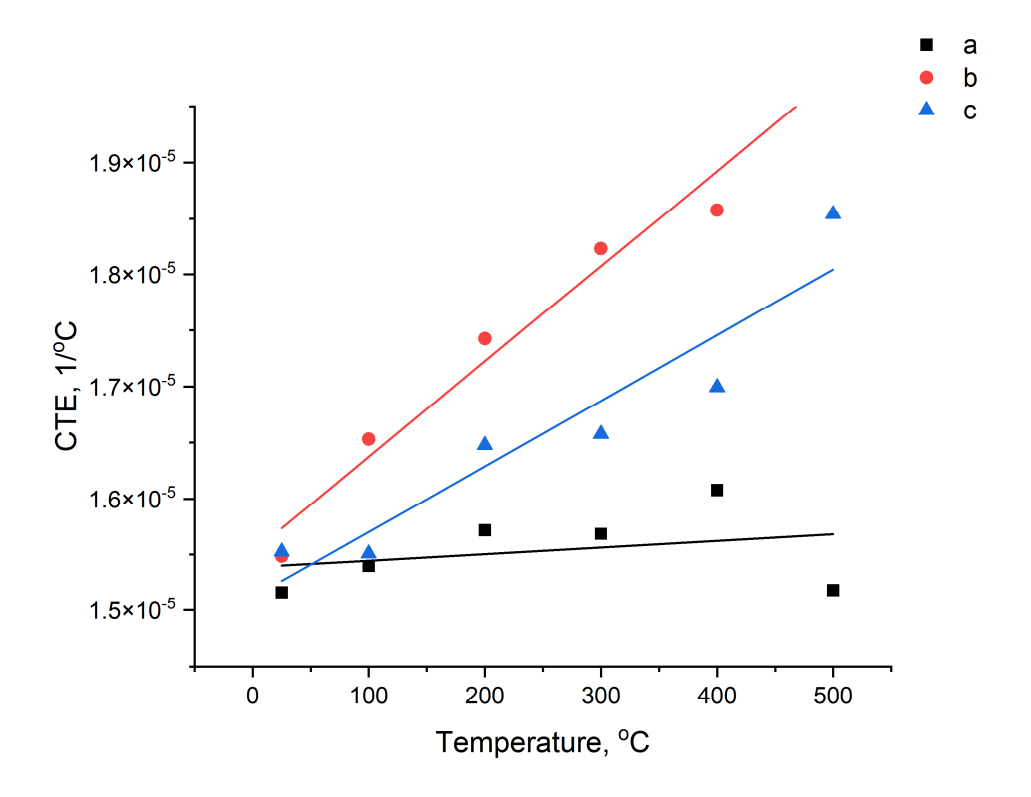


Figure 8. Directional dependent CTE from the bulk Al<sub>11</sub>Ce<sub>3</sub> showing anisotropic behavior

A pure, bulk  $Al_{11}Ce_3$  sample was arc melted from a mixture of stoichiometric Al ad Ce powders and the CTE measured with the same conditions as the thin films. The bulk  $Al_{11}Ce_3$  (123) results are included in figure 7 and shows a slight CTE temperature dependence in the temperature range of study varying roughly linearly from ~1.5x10<sup>-5</sup>/°C to 1.72x10<sup>-5</sup>/°C, from room temperature to 550°C. A Rietveld analysis of the entire XRD pattern (shown in supplemental information) demonstrated a slight anisotropic behavior as shown in figure 8. The expansion of the a lattice parameter remains roughly stable at ~1.54x10<sup>-5</sup>/°C while the b lattice parameter

expands with a slightly higher slope, and the c lattice parameter expansion shows an even higher change from ~1.5x10<sup>-5</sup>/°C to 2.0x10<sup>-5</sup>/°C, from room temperature to 550°C. The refined lattice parameter values with respect to temperature is shown in supplement. Since the thin film sample demonstrates preferred orientation along the (123) plane, the expansion of the film is dominated by the a lattice parameter which is consistent with the nearly constant CTE in (123) reflection of the thin film. Similarly, analysis of the expansion of the bulk sample along the (040) and (006) planes are consistent with the b and c lattice parameter expansion, respectively. In addition, bulk samples with nominally 1 wt.% plus or minus the Al<sub>11</sub>Ce<sub>3</sub> composition were also generated. The measured CTE values of these samples were also consistent with both the Al and Al<sub>11</sub>Ce<sub>3</sub> phase in the thin films and this HTXRD data given in the supplement information.

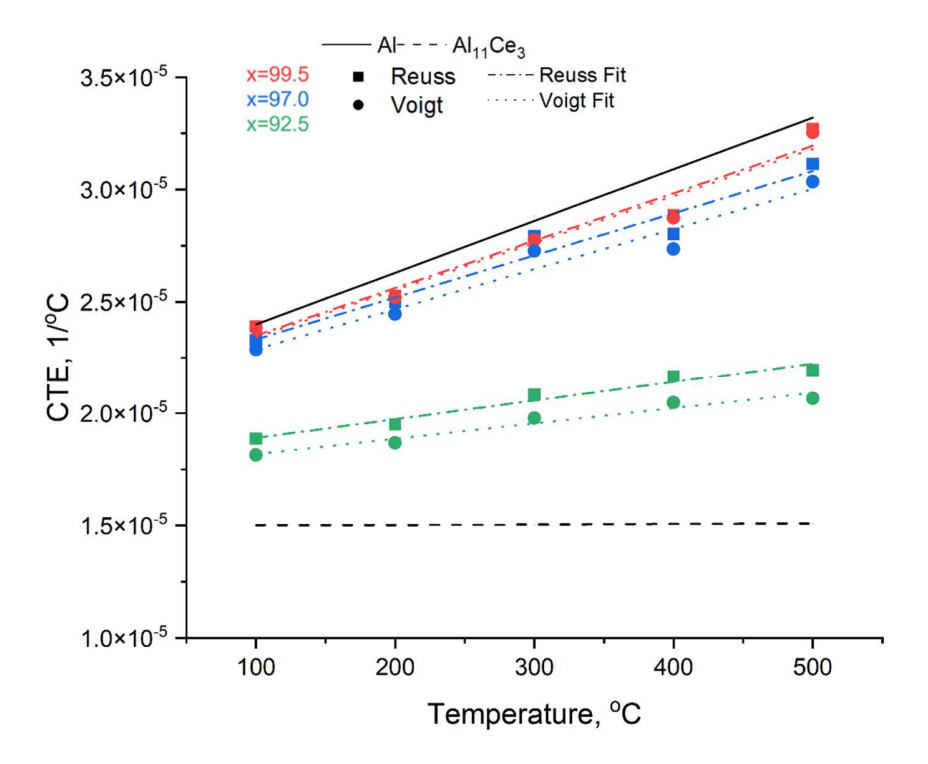


Figure 9. Two phase alloy composite CTE calculated from Voigt and Reuss approximations using average of our Al and Al<sub>11</sub>Ce<sub>3</sub> data as reference

The two phase alloy CTE was estimated using two rule of mixture models assuming uniform stress or strain. The Reuss [31] model for the effective coefficient of thermal expansion,  $\alpha^*$ , is given by

$$\alpha^* = \xi_1 \alpha_1 + \xi_2 \alpha_2$$
 (3)

where  $\xi_i$  and  $\alpha_i$  are the phase fractions and single phase coefficient of thermal expansions, respectively. The Voigt [32] upper bound model is given by

$$\alpha^* = \frac{\xi_1 E_1 \alpha_1 + \xi_2 E_2 \alpha_2}{\xi_1 E_1 + \xi_2 E_2} (4)$$

where E is the Young's Modulus for the respective phase taken to be 69 GPa for Al and a value of 97 GPa for  $Al_{11}Ce_3$  was extracted from figure 4 of Sims *et. al.* Figure 9 shows the two-phase alloy CTE as a function of temperature for various  $Al_xCe_{100-x}$  compositions. The  $Al_{11}Ce_3$  intermetallic CTE lowers the Al CTE and is suitable for some piston applications. Future work will be done to examine the two-phase system CTE via microfabricated cantilevers [33,34] structures and dilatometry for the thin film and bulk alloys, respectively.

# 4. Conclusion

The crystal structure and phase fraction, film morphology, electrical resistivity, and temperaturedependent coefficients of thermal expansion are all correlated to the Al<sub>x</sub>Ce<sub>100-x</sub> composition. In the as-deposited state, the Al (111) peak is present. Peak broadening and shifting indicate the formation of a metastable solid solution. Upon annealing, the α-Al<sub>11</sub>Ce<sub>3</sub> intermetallic phase forms and the Al (111) to α-Al<sub>11</sub>Ce<sub>3</sub> (123) peak ratio decreases as expected with increasing Ce content. The film transitions from an almost pure Al matrix to pure α-Al<sub>11</sub>Ce<sub>3</sub> intermetallic across the material library sputter deposited on the SiO<sub>2</sub>-coated Si wafer. The as-deposited resistivity increases with increasing Ce content, consistent with solid solution alloying. In the annealed sample, the resistivity is lower, however the two-phase system resistivity increases with increasing Ce content due to the reduction in the percolating network with the precipitation and increasing phase fraction of the intermetallic phase. Additionally, we investigated the temperature dependent CTE at a series of fixed alloy compositions. The two phases expanded independently of one another with the Al matrix having a temperature-dependent CTE similar to bulk Al, and the Al<sub>11</sub>Ce<sub>3</sub> intermetallic phase showing a constant CTE of ~1.5x10<sup>-5</sup>/°C in the range of study. The two-phase alloy CTE was estimated via the Reuss and Voigt models and with the Al<sub>11</sub>Ce<sub>3</sub> CTE being lower than Al, it suppresses the composite CTE value bring it in line with the current premium piston alloys that are commercially available. Importantly, we have demonstrated the efficacy of the thin film technique, which is consistent with the bulk alloy, thus we can explore more complex multi-component alloys via the thin film combinatorial synthesis and XRD analysis technique for rapid discovery of new lower CTE materials.

## Acknowledgements

This research was sponsored by the Critical Materials Institute, an Energy Innovation Hub funded by the U.S. Department of Energy (DOE), Office of Energy Efficiency and Renewable Energy, Advanced Manufacturing Office and Eck Industries. This work was performed under the auspices of the U.S. DOE.

#### References

- [1] E.T. Stromme, H.B. Henderson, Z.C. Sims, M.S. Kesler, D. Weiss, R.T. Ott, F. Meng, S. Kassoumeh, J. Evangelista, G. Begley, O. Rios, Ageless Aluminum-Cerium-Based Alloys in High-Volume Die Casting for Improved Energy Efficiency, JOM. 70 (2018) 866–871. https://doi.org/10.1007/s11837-018-2861-9.
- [2] Z.C. Sims, O.R. Rios, D. Weiss, P.E.A. Turchi, A. Perron, J.R.I. Lee, T.T. Li, J.A. Hammons, M. Bagge-Hansen, T.M. Willey, K. An, Y. Chen, A.H. King, S.K. McCall, High performance aluminum–cerium alloys for high-temperature applications, Mater. Horiz. 4 (2017) 1070–1078. https://doi.org/10.1039/C7MH00391A.
- [3] Z.C. Sims, D. Weiss, S.K. McCall, M.A. McGuire, R.T. Ott, T. Geer, O. Rios, P.A.E. Turchi, Cerium-Based, Intermetallic-Strengthened Aluminum Casting Alloy: High-Volume Co-product Development, JOM. 68 (2016) 1940–1947. https://doi.org/10.1007/s11837-016-1943-9.
- [4] J. Stroh, D. Sediako, D. Weiss, Development of Cerium-Reinforced Specialty Aluminum Alloy with Application of X-ray and Neutron Diffraction, Int. J. Met. 15 (2021) 29–39. https://doi.org/10.1007/s40962-020-00467-6.
- [5] D. Weiss, High Performance Aluminum Casting Alloys for Engine Applications, SAE International, Warrendale, PA, 2016. https://doi.org/10.4271/2016-32-0019.
- [6] M.A. Domínguez-Crespo, A.M. Torres-Huerta, S.E. Rodil, E. Ramírez-Meneses, G.G. Suárez-Velázquez, M.A. Hernández-Pérez, Effective corrosion protection of AA6061 aluminum alloy by sputtered Al–Ce coatings, Electrochimica Acta. 55 (2009) 498–503. https://doi.org/10.1016/j.electacta.2009.09.002.
- [7] M.A. Domínguez-Crespo, S.E. Rodil, A.M. Torres-Huerta, E. Ramírez-Meneses, G. Suárez-Velázquez, Structural and electrochemical performance of sputtered Al–Ce films on AA6061 aluminum alloy substrates, Surf. Coat. Technol. 204 (2009) 571–579. https://doi.org/10.1016/j.surfcoat.2009.08.041.
- [8] A.C. Crossland, G.E. Thompson, P. Skeldon, G.C. Wood, C.J.E. Smith, H. Habazaki, K. Shimizu, Anodic Oxidation of Al-Ce Alloys and Inhibitive Behaviour of Cerium Species, Corros. Sci. 40 (1998) 871–885.
- [9] E.R. Jette, F. Foote, Precision Determination of Lattice Constants, J. Chem. Phys. 3 (1935) 605–616. https://doi.org/10.1063/1.1749562.
- [10] A.W. Lawson, T.-Y. Tang, Concerning the High Pressure Allotropic Modification of Cerium, Phys. Rev. 76 (1949) 301–302. https://doi.org/10.1103/PhysRev.76.301.
- [11] F. Czerwinski, Thermal stability of aluminum–cerium binary alloys containing the Al–Al11Ce3 eutectic, Mater. Sci. Eng. A. 809 (2021) 140973. https://doi.org/10.1016/j.msea.2021.140973.
- [12] O. Kraft, W.D. Nix, Measurement of the lattice thermal expansion coefficients of thin metal films on substrates, J. Appl. Phys. 83 (1998) 3035–3038. https://doi.org/10.1063/1.367118.
- [13] Y. Kuru, M. Wohlschlögel, U. Welzel, E.J. Mittemeijer, Coefficients of thermal expansion of thin metal films investigated by non-ambient X-ray diffraction stress analysis, Surf. Coat. Technol. 202 (2008) 2306–2309. https://doi.org/10.1016/j.surfcoat.2007.08.002.
- [14] C.-L. Chen, R.C. Thomson, Study on thermal expansion of intermetallics in multicomponent Al–Si alloys by high temperature X-ray diffraction, Intermetallics. 18 (2010) 1750–1757. https://doi.org/10.1016/j.intermet.2010.05.015.

- [15] P. Staron, A. Stark, N. Schell, P. Spoerk-Erdely, H. Clemens, Thermal Expansion of a Multiphase Intermetallic Ti-Al-Nb-Mo Alloy Studied by High-Energy X-ray Diffraction, Materials. 14 (2021) 727. https://doi.org/10.3390/ma14040727.
- [16] G. Rodrigues, C.A. Nunes, P.A. Suzuki, G.C. Coelho, Thermal expansion of the Ti5Si3 and Ti6Si2B phases investigated by high-temperature X-ray diffraction, Intermetallics. 14 (2006) 236–240. https://doi.org/10.1016/j.intermet.2005.05.007.
- [17] R. Collette, Y. Wu, P.D. Rack, Correlating the optical property evolution in the Au-Ni binary thin films: From metastable solid solution to phase separated alloy, J. Alloys Compd. 793 (2019) 695–704. https://doi.org/10.1016/j.jallcom.2019.04.207.
- [18] W.L. Boldman, D.A. Garfinkel, R. Collette, C.S. Jorgenson, D.K. Pradhan, D.A. Gilbert, P.D. Rack, Exploring the composition, phase separation and structure of AgFe alloys for magneto-optical applications, Mater. Sci. Eng. B. 266 (2021) 115044. https://doi.org/10.1016/j.mseb.2021.115044.
- [19] Y. Wu, C. Liu, T.M. Moore, G.A. Magel, D.A. Garfinkel, J.P. Camden, M.G. Stanford, G. Duscher, P.D. Rack, Exploring Photothermal Pathways via in Situ Laser Heating in the Transmission Electron Microscope: Recrystallization, Grain Growth, Phase Separation, and Dewetting in Ag0.5Ni0.5 Thin Films, Microsc. Microanal. 24 (2018) 647–656. https://doi.org/10.1017/S1431927618015465.
- [20] E.J. Sullivan, J.A. Tomko, J.M. Skelton, J.M. Fitz-Gerald, P.E. Hopkins, J.A. Floro, Lamellar instabilities during scanning laser melting of Al–Cu eutectic and hypoeutectic thin films, J. Alloys Compd. 865 (2021) 158800. https://doi.org/10.1016/j.jallcom.2021.158800.
- [21] J.D. Fowlkes, J.M. Fitz-Gerald, P.D. Rack, Ultraviolet emitting (Y1–xGdx)2O3–δ thin films deposited by radio frequency magnetron sputtering: Combinatorial modeling, synthesis, and rapid characterization, Thin Solid Films. 510 (2006) 68–76. https://doi.org/10.1016/j.tsf.2005.12.309.
- [22] F. Czerwinski, B. Shalchi Amirkhiz, On the Al–Al11Ce3 Eutectic Transformation in Aluminum–Cerium Binary Alloys, Materials. 13 (2020) 4549. https://doi.org/10.3390/ma13204549.
- [23] D. Weiss, "Castability and Characteristics of High Cerium Aluminum Alloys | IntechOpen," Dec. 2017, Accessed: Apr. 04, 2022. [Online]. Available: https://www.intechopen.com/chapters/58487
- [24] D.N. Lee, Textures and structures of vapor deposits, J. Mater. Sci. 34 (1999) 2575–2582.
- [25] J. Peltonen, M. Murtomaa, K. Robinson, J. Salonen, The electrical resistivity and relative permittivity of binary powder mixtures, Powder Technol. 325 (2018) 228–233. https://doi.org/10.1016/j.powtec.2017.10.060.
- [26] R.A. Serway, in: Princ. Phys., 2nd ed., Saunders College Pub., Fort Worth, Texas, 1998: p. 602.
- [27] C. S. Garde, T. Takeuchi, Y. Nakano, Y. Takeda, Y. Ota, Y. Miyauchi, K. Sugiyama, M. Hagiwara, K. Kindo, F. Honda, R. Settai, Y. Ōnuki, Electrical and Magnetic Properties of R <sup>3</sup> Al <sub>11</sub> (R = La, Ce, Pr, and Nd), J. Phys. Soc. Jpn. 77 (2008) 124704. https://doi.org/10.1143/JPSJ.77.124704.
- [28] Y. Zoo, D. Adams, J.W. Mayer, T.L. Alford, Investigation of coefficient of thermal expansion of silver thin film on different substrates using X-ray diffraction, Thin Solid Films. 513 (2006) 170–174. https://doi.org/10.1016/j.tsf.2006.02.005.
- [29] W. Fang, C.-Y. Lo, On the thermal expansion coefficients of thin films, Sens. Actuators Phys. 84 (2000) 310–314. https://doi.org/10.1016/S0924-4247(00)00311-3.

- [30] A.J.C. Wilson, The thermal expansion of aluminium from 0 to 650 C, Proc. Phys. Soc. 53 (1941) 235–244. https://doi.org/10.1088/0959-5309/53/3/305.
- [31] A. Reuss, Berechnung der Fließgrenze von Kristallen auf Grund der Plastizitätsbedingung für Einkristalle, Z. Für Angew. Math. Mech. 9 (1922) 49–58.
- [32] W. Voigt, Theoretische Studien über die Elastizitätsverhältnisse der Krystalle, Ann. Phys. 274 (1889) 573–587.
- [33] M. Toda, N. Inomata, T. Ono, I. Voiculescu, Cantilever beam temperature sensors for biological applications, IEEJ Trans. Electr. Electron. Eng. 12 (2017) 153–160. https://doi.org/10.1002/tee.22360.
- [34] L. Saturday, L. Wilson, S. Retterer, N.J. Evans, D. Briggs, P.D. Rack, N. Lavrik, Thermal conductivity of nano- and micro-crystalline diamond films studied by photothermal excitation of cantilever structures, Diam. Relat. Mater. 113 (2021) 108279. https://doi.org/10.1016/j.diamond.2021.108279.